

Precise determination of the low-energy electronuclear Hamiltonian of $\text{LiY}_{1-x}\text{Ho}_x\text{F}_4$

A. Beckert^{1,2,*}, M. Grimm^{2,3}, R. I. Hermans⁴, J. R. Freeman⁵, E. H. Linfield⁵, A. G. Davies⁵, M. Müller³,
H. Sigg¹, S. Gerber¹, G. Matmon¹ and G. Aeppli^{2,6,7,8}

¹Laboratory for X-Ray Nanoscience and Technologies, Paul Scherrer Institut, CH-5232 Villigen PSI, Switzerland

²Laboratory for Solid State Physics, ETH Zurich, CH-8093 Zurich, Switzerland

³Laboratory for Theoretical and Computational Physics, Paul Scherrer Institut, CH-5232 Villigen PSI, Switzerland


⁴London Centre for Nanotechnology, University College London, London WC1H 0AH, United Kingdom

⁵School of Electronic and Electrical Engineering, University of Leeds, Leeds LS9 2JT, United Kingdom

⁶Photon Science Division, Paul Scherrer Institut, CH-5232 Villigen PSI, Switzerland

⁷Institute of Physics, EPF Lausanne, CH-1015 Lausanne, Switzerland

⁸Quantum Center, ETH Zurich, CH-8093 Zurich, Switzerland

 (Received 17 December 2020; revised 7 July 2022; accepted 24 August 2022; published 12 September 2022)

The insulating rare-earth magnet $\text{LiY}_{1-x}\text{Ho}_x\text{F}_4$ has received great attention because a laboratory field applied perpendicular to its crystallographic c axis converts the low-energy electronic spin Hamiltonian into the (dilute) transverse field Ising model. The mapping between the real magnet and the transverse field Ising model is strongly dependent on the exact nature of the low-energy Hamiltonian for the material, which can be determined by spectroscopy in the dilute limit. The energies of the eigenstates are in the difficult terahertz (THz) regime, and here we use THz time domain and Fourier transform spectroscopy to directly measure the lowest crystal-field levels of $\text{LiY}_{1-x}\text{Ho}_x\text{F}_4$ in the dilute limit, including nuclear hyperfine substructure. The high resolution of our measurements allows us to observe the nonquidistantly spaced Ho ($I = \frac{7}{2}$) hyperfine transitions originating from dipolar and quadrupolar hyperfine interactions. We provide refined crystal-field parameters and extract the dipolar and quadrupolar hyperfine constants $A_J = 0.027\,03 \pm 0.000\,03 \text{ cm}^{-1}$ ($810.3 \pm 0.9 \text{ MHz}$) and $B = 0.04 \pm 0.01 \text{ cm}^{-1}$ ($1.2 \pm 0.3 \text{ GHz}$), respectively. Thereupon we determine all crystal-field energy levels and magnetic moments of the 5I_8 ground-state manifold, including the (nonlinear) hyperfine corrections. The latter improve the prediction precision by a factor of 60 compared to previous crystal-field parameters. Additionally, we establish the far-infrared, low-temperature refractive index of $\text{LiY}_{1-x}\text{Ho}_x\text{F}_4$.

DOI: [10.1103/PhysRevB.106.115119](https://doi.org/10.1103/PhysRevB.106.115119)

I. INTRODUCTION

The $\text{LiY}_{1-x}\text{Ho}_x\text{F}_4$ dilution series has been a fertile venue for quantum phenomena, including single-ion tunneling in the very dilute limit [1], quantum phase transitions to both ferromagnetic [2,3] and quantum glass states [4–6], ferromagnetic domain wall tunneling [7], quantum Griffiths effects [8], as well as an entangled low-temperature state [9] with extraordinarily sharp low-frequency collective modes revealed by spectral hole burning [10–12]. In addition, over two decades ago, experiments [13] on the material showed the potential of quantum annealing for solving optimization problems, and so spawned adiabatic quantum computing.

The isostructural nature of the dilution series from ferromagnetic LiHoF_4 to nonmagnetic LiYF_4 allows for consistent mapping of the effective low-energy electronic Hamiltonian in relatively small laboratory fields to the “classic” (dilute) transverse field Ising model across a range of concentrations x (for a review see Ref. [14]). While such a purely electronic model captures much of the essential physics (also at zero applied field where the dipolar interaction between Ho ions can induce internal transverse fields), it does not suffice for a

detailed description, neither of the quantum phase transition in pure LiHoF_4 nor of the hole burning [10–12] at intermediate x . This fact was recognized long ago both by the original experimentalists [3] as well as theorists [15,16]. In particular, this is because the Ho atoms carry nuclear spins $I = \frac{7}{2}$ with a large hyperfine (HF) coupling to the electronic moments. Furthermore, laboratory fields mix relatively low-lying crystal-field (CF) states to split the ground state into the two levels of the simple transverse field Ising model, and so the effective transverse field explicitly depends on the low-energy CF states. Therefore, exact knowledge of them and the hyperfine Hamiltonian is required to understand the low-energy physics of $\text{LiY}_{1-x}\text{Ho}_x\text{F}_4$ and to investigate its quantum statistical mechanics.

Owing to experimental challenges in the terahertz (THz) regime where the relevant CF excitations are found, comprehensive low-energy, high-resolution data for $\text{LiY}_{1-x}\text{Ho}_x\text{F}_4$ and corresponding CF parameters have not been available so far [17–20]. Here we perform low-temperature THz time-domain spectroscopy (TDS) and synchrotron-based ultrahigh-resolution Fourier transform infrared (FTIR) spectroscopy (Sec. II) to (re)examine the transitions between the three lowest-lying CF levels of the 5I_8 ground-state manifold of $\text{LiY}_{1-x}\text{Ho}_x\text{F}_4$. In addition, we use previous treatments of nuclear spins coupled to electronic CF states (e.g., in

*adrian.beckert@psi.ch

Refs. [21,22]) up to second order in the dipolar interaction, and to first order in the quadrupolar coupling in Sec. III to describe our data. We also include energy shifts due to ${}^6\text{Li}$ and ${}^7\text{Li}$ isotopes. We extract CF parameters by combining our data with CF energy measurements of the 5I_8 manifold from Ref. [20], which enables us to refine the dipolar HF interaction constant A_J in Sec. IV. Based on the resulting CF parameters, we predict all 5I_8 CF energies and their magnetic moments. The high instrumental resolution allows us also to determine the quadrupolar HF constant B . Using B and A_J , we infer nonequidistant HF corrections of the three CF levels involved in our measurements, including the ground state. We provide an approximation of these HF corrections based on our measurement results, which corroborate our numerical simulation. We compare CF energy predictions from our CF parameters to predictions from literature values in Sec. V, revealing an improved precision by more than an order of magnitude. Finally, in Appendix A we provide a refractive index measurement of $\text{LiY}_{1-x}\text{Ho}_x\text{F}_4$ from 70 to 5 cm^{-1} corresponding to $\sim 2\text{ THz}$ to the sub-THz range, which will be useful for designing future optical experiments and devices. A summary and an outlook are found in Sec. VI.

II. EXPERIMENTAL SETUP

A. Sample

We study three commercially available $\text{LiY}_{1-x}\text{Ho}_x\text{F}_4$ single crystals at the low doping concentrations of $x = 1\%$, 0.1% , and 0.01% . Ho^{3+} ions substitute for the Y^{3+} ions in the Scheelite crystal structure (space group C_{4h}^6) of LiYF_4 having the local point symmetry group S_4 . For an overview of the physical properties and studies of $\text{LiY}_{1-x}\text{Ho}_x\text{F}_4$ as a function of doping concentration x , external magnetic fields, and temperature we refer to Refs. [20,23].

The crystal dimensions along the light propagation direction are chosen such that transmission is optimized for each x . Samples were mounted on the cold finger of a continuous-flow liquid-helium cryostat. The THz light was linearly polarized. The sample was oriented with the crystallographic c axis parallel or perpendicular to the magnetic field component to satisfy selection rules for magnetic dipole transitions, while the propagation direction was always perpendicular to c . All reported temperatures denote the nominal values at the cryostat cold finger.

B. Experimental methods

We use two different methods: First, TDS was conducted on $\text{LiY}_{1-x}\text{Ho}_x\text{F}_4$ ($x = 0.1\%$) for wave numbers $\tilde{\nu} < 10\text{ cm}^{-1}$ (300 GHz), as well as for refractive-index measurements of the $x = 1\%$ crystal for $\tilde{\nu} \leq 70\text{ cm}^{-1}$ (2.1 THz). Figure 1 shows a schematic of the custom experimental setup, which is based on an 800-nm laser, delivering 100-fs pulses at 80-MHz repetition rate. The beam is split, directing 250 mW through a variable delay line. This fraction of the laser is focused onto a low-temperature grown GaAs photoconductive emitter with a $100\text{-}\mu\text{m}$ electrode gap (biased at 100 V, 7.3 kHz) that generates a linearly polarized single-cycle THz pulse. The THz pulse is then collected from the back of the emitter substrate with a Si hyperhemispheric lens and focused onto

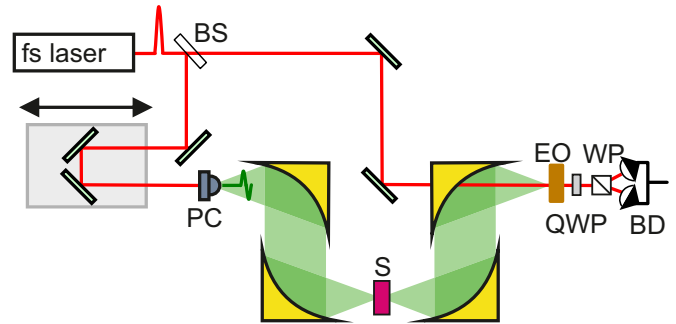


FIG. 1. Schematic of the TDS setup showing the femtosecond (fs) laser, the beam splitter (BS), a photoconductive (PC) antenna, the sample (S), a ZnTe electro-optic (EO) sampling crystal, a quarter-wave plate (QWP), a Wollaston prism (WP), and balanced photodiodes (BD) for detection.

the sample with a parabolic mirror. Thereafter, the transmitted beam is refocused onto a 2-mm-thick ZnTe crystal for electro-optic sampling. In this detection scheme, the THz branch is overlapped with the 800-nm branch. As a function of delay time, the polarization change of the transmitted 800-nm light is then proportional to the instantaneous THz field in the ZnTe crystal. The signal is measured using balanced photodiodes and a lock-in amplifier referenced to the emitter bias frequency. Fourier transforms of the delay scans then yield the spectra.

Second, ultrahigh-resolution FTIR spectroscopy was conducted on $\text{LiY}_{1-x}\text{Ho}_x\text{F}_4$ ($x = 0.01\%$) for $\tilde{\nu} > 15\text{ cm}^{-1}$ (450 GHz) using a custom-built Bruker FTIR spectrometer with 0.00077 cm^{-1} (23 MHz) resolution. A He-flow cryostat for low-temperature measurements was fitted to the spectrometer. The Swiss Light Source at the Paul Scherrer Institut, Switzerland, provides high-brilliance and strongly polarized far-infrared (FIR) radiation. Reference [24] provides more details about the FTIR instrument. The unique combination of a low-temperature, ultrahigh-resolution spectrometer and FIR/THz synchrotron radiation allowed us to measure the absorbance spectra with a resolution of up to 10^{-3} cm^{-1} (30 MHz), which is more than an order of magnitude higher than previously reported measurements within the 5I_8 ground state-manifold [17–20] and at least double the resolution of measurements involving excited-state manifolds [20,25–27].

The THz response of the holmium ions (Ho^{3+}) in the LiYF_4 matrix is characterized by referencing the sample absorption at low temperature to a higher-temperature measurement. This ensures that both the background absorption of the crystal host and temperature-independent reflections from the sample and the experimental setup are removed. Therefore, we show absorbance spectra $A(\tilde{\nu}) = \log_{10}[I_0(\tilde{\nu})/I(\tilde{\nu})]$ as a function of wave number $\tilde{\nu}$ (cm^{-1}), with $I(\tilde{\nu})$ [$I_0(\tilde{\nu})$] denoting the wave-number-dependent sample (reference) transmission.

III. CRYSTAL-FIELD TRANSITIONS WITH HYPERFINE INTERACTIONS

Our high-resolution instruments enable us to resolve the HF structure of the measured CF states to high precision;

analysis methods which take advantage of this structure are described in Ref. [28]. We turn now to the theoretical understanding of the HF corrections to the measured CF states. In this paper we denote a transition from an initial CF state i to a final state f by $i \rightarrow f$. Further, we label the 5I_8 ground-state manifold states $8.n$ according to their CF energy E_n : the ground state (8.1, $E_1 = 0$) is a doublet (under time-reversal symmetry) and carries $\Gamma_{3,4}$ symmetry, the first-excited (8.2) and second-excited (8.3) states have Γ_2 symmetry at $E_2 = 6.8 \text{ cm}^{-1}$ (205 GHz) and $E_3 = 23.3 \text{ cm}^{-1}$ (699 GHz), respectively. We denote the CF symmetries (irreducible representations) by Γ_j , $j \in \{1, 2, 3, 4\}$, using standard conventions. Individual HF states are labeled as $|8.n^\sigma, m_z\rangle \equiv |8.n^\sigma\rangle \otimes |m_z\rangle$, where $\sigma = -1$ ($\sigma = +1$) denotes the Γ_3 (Γ_4) state if the n th level belongs to a doublet. m_z is the nuclear spin projection onto the crystallographic c axis in the unperturbed electron-nuclear wave function.

A. Hyperfine interaction in perturbation theory

Within the lowest J multiplet, the electrons of each Ho^{3+} ion ($J = 8$) couple to their nuclear spin ($I = \frac{7}{2}$) via the dipolar and quadrupolar HF interactions

$$\begin{aligned} H_{\text{HF}} &= H_{\text{HF,dip}} + H_{\text{HF,quad}} \\ &= A_J \vec{J} \cdot \vec{I} + \frac{B}{2I(2I-1)J(2J-1)} \\ &\quad \times \left(3(\vec{J} \cdot \vec{I})^2 + \frac{3}{2}(\vec{J} \cdot \vec{I}) - I(I+1)J(J+1) \right), \quad (1) \end{aligned}$$

with the dipolar and quadrupolar coupling constants A_J and B , respectively [29,30]. We consider effects of A_J up to second order and B to first order because of the relative size of these terms. We neglect HF corrections due to coupling of the nuclear electric quadrupole moment to the electric field gradient. Using the literature value in Ref. [31], this effect is estimated to be an order of magnitude smaller than the terms in Hamiltonian (1).

Using perturbation theory as in Ref. [30], the ground-state energy corrections $\delta_{8.1^\sigma, m_z}$ of the states $|8.1^\sigma, m_z\rangle$ are

$$\begin{aligned} \delta_{8.1^+, +m_z} &= \delta_{8.1^-, -m_z} = A_J \langle 8.1^+ | J_z | 8.1^+ \rangle m_z \\ &+ \sum_{j \in \Gamma_1} \frac{A_j^2}{4\Delta E_{1j}} [|\langle 8.j | J_+ | 8.1^+ \rangle|^2 [I(I+1) - m_z(m_z - 1)]] \\ &+ \sum_{j \in \Gamma_2} \frac{A_j^2}{4\Delta E_{1j}} [|\langle 8.j | J_- | 8.1^+ \rangle|^2 [I(I+1) - m_z(m_z + 1)]] \\ &+ \sum_{\substack{j \in \Gamma_{3,4} \\ j \neq 1}} \frac{A_j^2}{\Delta E_{1j}} [|\langle 8.j^+ | J_z | 8.1^+ \rangle|^2 m_z^2] \\ &+ \frac{B \langle 8.1^+ | 3J_z^2 - J(J+1) | 8.1^+ \rangle}{4I(2I-1)J(2J-1)} [3m_z^2 - I(I+1)], \quad (2) \end{aligned}$$

and the corrections of the first two excited electronic states ($n = 2, 3$) are

$$\begin{aligned} \delta_{8.n, \pm m_z} &= \sum_{\substack{j \in \Gamma_2 \\ j \neq n}} \frac{A_j^2}{\Delta E_{nj}} |\langle 8.j | J_z | 8.n \rangle|^2 m_z^2 \\ &+ \sum_{j \in \Gamma_{3,4}} \frac{A_j^2}{2\Delta E_{nj}} g [|\langle 8.j^+ | J_+ | 8.n \rangle|^2 [I(I+1) - m_z^2]] \\ &+ \frac{B \langle 8.n | 3J_z^2 - J(J+1) | 8.n \rangle}{4I(2I-1)J(2J-1)} [3m_z^2 - I(I+1)]. \quad (3) \end{aligned}$$

Here $\Delta E_{nj} = E_n - E_j$ is the energy difference between the CF levels $|8.n\rangle$ and $|8.j\rangle$. The sums run over all CF states $|8.j\rangle$ carrying the irreducible representations Γ_i , $i \in \{1, 2, 3, 4\}$. From now on, we use the abbreviation $\lambda_n/2$ for the prefactor of the HF corrections $\propto m_z^2$ of the CF states $8.n$.

These perturbative corrections are sufficient to interpret the HF spectrum of the 8.1, 8.2, and 8.3 states. Due to the absence of external magnetic fields, by Kramers' theorem all HF states are doubly degenerate with their time-reversed state (under time reversal: $m_z \rightarrow -m_z$, $\sigma \rightarrow -\sigma$). The electronic doublet 8.1, which is Ising type with a moment along the crystallographic c axis (due to the S_4 site symmetry [23]), experiences a dominant first-order shift $\propto \sigma A_J m_z$ that leads to an equidistant HF splitting into eight HF Kramers doublets. In the lowest ($\sigma m_z = -\frac{7}{2}$) and highest ($\sigma m_z = +\frac{7}{2}$) of these HF states the electronic and magnetic moments are antialigned and aligned, respectively. The singlets do not undergo a first-order HF shift in A_J due to their vanishing moment. Within a single CF state, the equidistance of the HF energies is broken by the second-order terms in A_J and first-order term in B , all leading to corrections $\propto m_z^2$. These corrections determine the relative order of the m_z states within a singlet; note that for the states 8.2 and 8.3, the relative order is reversed. The dominant correction due to the small energy denominator in Eq. (3) comes from the mutual repulsion of these singlets caused by the dipolar HF interaction. An illustration of the HF levels of the 8.2 and 8.3 states is shown in Fig. 4.

B. Experiments

We measure the transmission of the $8.1 \rightarrow 8.2$ magnetic dipole transition in $\text{LiY}_{1-x}\text{Ho}_x\text{F}_4$ ($x = 0.1\%$) at a temperature of $T = 2.9 \text{ K}$ by TDS with an instrument resolution of 0.017 cm^{-1} (500 MHz). The absorbance is shown in Fig. 2(a), where we directly resolve an eightfold, approximately equidistant HF splitting of $\sim 0.146 \text{ cm}^{-1}$ (4.4 GHz), which reflects the dominant linear HF shift of the ground-state doublet 8.1. The deviation of the individual line intensities from a Boltzmann distribution (cf. Refs. [19,20]) originates from sample- and setup-specific systematic errors such as residual interference of optical components. The extracted Gaussian full width at half-maximum (FWHM) of a single HF line is $0.017 \pm 0.001 \text{ cm}^{-1}$ ($510 \pm 30 \text{ MHz}$) and thus instrument-resolution limited.

The absorbance of the $8.1 \rightarrow 8.3$ magnetic dipole transition of $\text{LiY}_{1-x}\text{Ho}_x\text{F}_4$ ($x = 0.01\%$) was measured at $T = 3.5 \text{ K}$ with FTIR spectroscopy and 0.001-cm^{-1} (30-MHz)

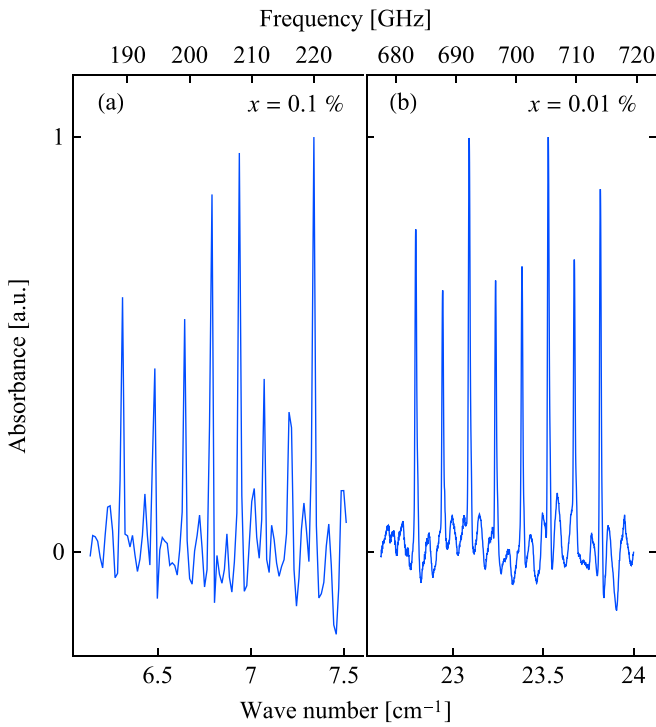


FIG. 2. Absorbance spectra of $\text{LiY}_{1-x}\text{Ho}_x\text{F}_4$ of (a) the $8.1 \rightarrow 8.2$ (TDS, $x = 0.1\%$, $T = 3$ K) and (b) the $8.1 \rightarrow 8.3$ (FTIR, $x = 0.01\%$, $T = 3.5$ K) transitions with conserved m_z .

resolution. The absorbance spectrum is shown in Fig. 2(b), also revealing the eightfold CF level splitting. The HF lines are nearly equidistant with a spacing of $\sim 0.146 \text{ cm}^{-1}$ (~ 4.4 GHz). The ultrahigh resolution of the FTIR spectrometer allows for a closer inspection of a single HF line. Figure 3 shows the sixth HF peak at $23.527 \pm 0.001 \text{ cm}^{-1}$

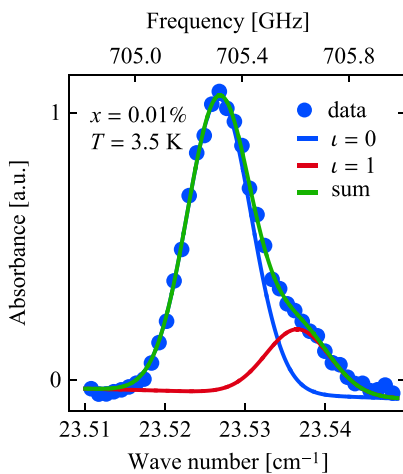


FIG. 3. Closeup of the asymmetric sixth $8.1 \rightarrow 8.3$ HF peak of $\text{LiY}_{1-x}\text{Ho}_x\text{F}_4$ ($x = 0.01\%$) at $T = 3.5$ K. The green line is a fit to the main peak (blue), attributed to the majority of Ho ions having $\iota = 0$ ${}^6\text{Li}$ neighbors, and the smaller second peak (red) that is shifted by isotopic splitting due to $\iota = 1$ ${}^6\text{Li}$ neighbors. A sinusoidal background owing to interference effects was subtracted with respect to the data shown in Fig. 2.

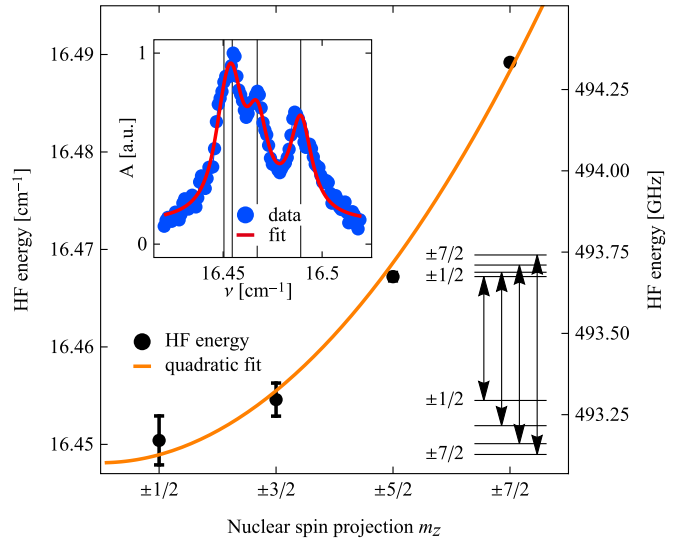


FIG. 4. HF shifts of the $8.2 \rightarrow 8.3$ transition as a function of the nuclear spin m_z . The shifts depend quadratically on m_z , as evidenced by the fit (orange). Note the degeneracy of $\pm m_z$ (see Table I). The top left inset shows the $8.2 \rightarrow 8.3$ absorbance of $\text{LiY}_{1-x}\text{Ho}_x\text{F}_4$ ($x = 0.01\%$) at $T = 9$ K (blue) and a fit to Lorentzian profiles (red). The vertical lines denote the peak center positions and correspond to the data in the main figure. Also shown on the bottom right is the energy-level diagram of the four observable $8.2 \rightarrow 8.3$ HF-split CF transitions.

(705.32 ± 0.03 GHz) in more detail. An asymmetry towards larger wave numbers is apparent, which is best explained by the isotopic splitting effect due to the natural abundance of ${}^6\text{Li}$ (7.6%) and ${}^7\text{Li}$ (92.4%). It was shown that if a number ι of lighter ${}^6\text{Li}$ atoms substitute the more abundant ${}^7\text{Li}$ in the immediate neighborhood of a Ho^{3+} ion, the CF parameters will be slightly shifted due to two possible mechanisms: virtual phonon exchanges between CF states and local lattice deformations [17,32,33]. In particular, Ref. [33] has shown that the latter effect is dominant in $\text{LiY}_{1-x}\text{Ho}_x\text{F}_4$. The anharmonicity of the lattice vibrations leads to an effective repulsion of the lighter ${}^6\text{Li}$ isotopes from their nearest neighbors due to the change in the mass as compared to ${}^7\text{Li}$. As a consequence, the F ions are shifted in position. Thus, whenever a ${}^6\text{Li}$ is near a Ho^{3+} ion, its CF is slightly changed and its energy levels are correspondingly shifted. This leads to additional peaks in the absorbance spectrum from Ho^{3+} ions with the number ι of less abundant ${}^6\text{Li}$ neighbors. Peaks associated with $\iota > 1$ or due to substitutions of more distant neighbors are too weak to be resolved. Thus, we only take the two strongest peaks $\iota = \{0, 1\}$ into account. By fitting two Gaussians, we find an isotopic splitting of $0.0098 \pm 0.0004 \text{ cm}^{-1}$ (294 ± 12 MHz) and a Gaussian FWHM of $0.0090 \pm 0.0001 \text{ cm}^{-1}$ (270 ± 3 MHz) for the individual peaks with the errors extracted from the covariance matrix. These findings are in agreement with the previously reported values of $0.0105 \pm 0.0015 \text{ cm}^{-1}$ (315 ± 45 MHz) [17] and the calculations in Ref. [33]. HF line energies of the $8.1 \rightarrow 8.3$ transition are always referred to the center of the dominant $\iota = 0$ peak.

Next we completed FTIR measurements of the $8.2 \rightarrow 8.3$ magnetic dipole transition of $\text{LiY}_{1-x}\text{Ho}_x\text{F}_4$ ($x = 0.01\%$) with

TABLE I. HF-split transition frequencies for CF level transitions $8.1 \rightarrow 8.2$ ($x = 0.1\%$), $8.1 \rightarrow 8.3$ ($x = 0.01\%$), and $8.2 \rightarrow 8.3$ ($x = 0.01\%$). All data are given in units of cm^{-1} and GHz. Uncertainties correspond to $\leq \pm 0.01$ (300), $\leq \pm 0.001$ (30), and $\leq \pm 0.003$ cm^{-1} (90 MHz) for the $8.1 \rightarrow 8.2$, $8.1 \rightarrow 8.3$, and $8.2 \rightarrow 8.3$ transitions, respectively.

Index	m_z	$8.1^+ \rightarrow 8.2$		$8.1^+ \rightarrow 8.3$		$8.2 \rightarrow 8.3$	
		cm^{-1}	(GHz)	cm^{-1}	(GHz)	cm^{-1}	(GHz)
1	-7/2	7.33	219.75	23.815	713.96	16.489	494.33
2	-5/2	7.21	216.15	23.671	709.64	16.467	493.67
3	-3/2	7.08	212.25	23.527	705.32	16.455	493.31
4	-1/2	6.94	208.06	23.381	700.94	16.450	493.16
5	+1/2	6.80	203.86	23.235	696.57	16.450	493.16
6	+3/2	6.64	199.06	23.088	692.16	16.455	493.31
7	+5/2	6.48	194.27	22.941	687.75	16.467	493.67
8	+7/2	6.31	189.17	22.794	683.35	16.489	494.33

0.002- cm^{-1} (60-MHz) resolution. The temperature was set to $T = 9$ K to thermally populate the 8.2 state. The inset of Fig. 4 shows the respective absorbance with a Lorentzian fit. The HF corrections $\propto m_z^2$ in Eq. (3) lead to an observable difference in the transition energies of the individual m_z states. The HF levels are also illustrated (not to scale) in Fig. 4. We fit the absorbance spectrum of the $8.2 \rightarrow 8.3$ transition with four Lorentzian profiles, taking the degeneracy of $\pm m_z$ into account. We allowed for different intensities and peak frequencies, but imposed an identical linewidth, which we found to be 0.013 ± 0.001 cm^{-1} (390 ± 30 MHz). Beyond a 0.008- cm^{-1} (240 MHz) constant offset, we obtain results that are consistent with the difference measured at the $8.1 \rightarrow 8.3$ and $8.1 \rightarrow 8.2$ transitions. We attribute the offset partly to the lower resolution of the TDS setup (0.017 cm^{-1} , 510 GHz) and systematic differences between the two experimental setups.

In Table I, we summarize the individual HF transition energies. Their centroid agrees with literature values which, however, provide the centroid only [17–20,22]. Note that the $8.1 \rightarrow 8.3$ ($x = 0.1\%$) transitions, obtained with FTIR, exhibit smaller uncertainties than the $8.1 \rightarrow 8.2$ ($x = 0.01\%$) transitions, since the latter was measured with lower instrument resolution of the TDS setup. Owing to the significant line overlap of the $8.2 \rightarrow 8.3$ ($x = 0.01\%$) transition data, the respective uncertainties extracted from the fit covariance matrix amount to ≤ 0.003 cm^{-1} (90 MHz). Reference [34] shows that increasing the rare-earth concentrations up to 10% does not noticeably affect the CF energies, which justifies a direct comparison of $x = 0.01\%$ and 0.1%.

IV. EXTRACTION OF CRYSTAL-FIELD PARAMETERS AND HYPERFINE INTERACTIONS

Previously, the CF parameters of $\text{LiY}_{1-x}\text{Ho}_x\text{F}_4$ have been estimated based on CF level energies obtained from the centroid of the HF structure due to the limited resolution [17,19,26,35,36], or by magnetic susceptibility measurements [37–39]. We improve on those earlier results by including the individually resolved HF energies of all three CF transitions reported here and supplement these data with results

TABLE II. CF parameters extracted from the transition energy measurements. We set $B_4^{-4} = 0$, which corresponds to an $\approx -11^\circ$ angle between the crystallographic a axis and the x axis, estimated from point charge calculations in Ref. [39].

CF parameter	Energy	
	cm^{-1}	(Hz)
B_2^0	$(-2.66 \pm 0.05) \times 10^{-1}$	$(-7.97 \pm 0.15) \times 10^9$
B_4^0	$(1.68 \pm 0.04) \times 10^{-3}$	$(5.04 \pm 0.12) \times 10^7$
B_4^4	$(2.81 \pm 0.02) \times 10^{-2}$	$(8.42 \pm 0.06) \times 10^8$
B_6^0	$(5.74 \pm 0.18) \times 10^{-6}$	$(1.72 \pm 0.54) \times 10^5$
B_6^4	$(5.60 \pm 0.03) \times 10^{-4}$	$(1.68 \pm 0.01) \times 10^7$
B_6^{-4}	$(0.00 \pm 3.84) \times 10^{-3}$	$(0.00 \pm 1.15) \times 10^8$

from higher-lying CF states from Ref. [20]. We fit the CF parameters and the HF coupling constant A_J simultaneously by numerically calculating the transition energies from the CF Hamiltonian (without HF interaction), as well as the HF splitting to first order in A_J . The transition energies are weighted with their measurement errors. This procedure only neglects small second-order corrections to the CF energies due to HF interactions [see Eqs. (2) and (3)]. The refined CF parameters are reported in Table II. We extract the HF coupling constant $A_J = 0.02703 \pm 0.00003$ cm^{-1} (810.3 ± 0.9 MHz) which is comparable to previous estimates in the literature of $A_J = 0.0282 \pm 0.0005$ [40] and 0.0270 ± 0.0003 cm^{-1} [41]. The errors of the CF parameters and A_J are computed from the covariance matrix.

In contrast to A_J , the determination of the quadrupolar HF interaction constant B requires precise knowledge of the deviations from the linear dipolar HF contributions. We utilize our high-resolution spectra ($8.1 \rightarrow 8.2$, $8.1 \rightarrow 8.3$, $8.2 \rightarrow 8.3$) to fit B separately, by using the determined CF parameters and A_J , and numerically calculating the full HF spectrum. We find $B = 0.04 \pm 0.01$ cm^{-1} (1.2 ± 0.3 GHz), which is comparable to the literature value $B = 0.059$ cm^{-1} (1.8 GHz) calculated for the free Ho atom [21].

The parameters A_J and B allow us to numerically compute the HF spectrum. We present a comparison to the experimental data in Fig. 5. To emphasize the HF corrections $\propto m_z^2$, we look at the difference D_n of transition frequencies $8.1 \rightarrow 8.n$ between neighboring m_z for $n = 2, 3$. From Eqs. (2) and (3) we expect $D_{2,3}$ to be linear in m_z (orange lines), with the slopes $s_{2,3}$ being a measure of the HF corrections $\propto m_z^2$. We find $s_2 = (7.2 \pm 0.5) \times 10^{-3}$ cm^{-1} (215 ± 15 MHz) and $s_3 = (6 \pm 1) \times 10^{-4}$ cm^{-1} (18 ± 3 MHz) based on a linear regression. The numerically calculated values are shown in violet (D_2) and cyan (D_3). On average, we find the deviations of the experimental and numerical values to be 16% for the 8.2 and only 1.5% for the 8.3 level, reflecting the respective measurement resolutions.

The experimental values of D_2 and D_3 allow an order-of-magnitude estimation of the m_z^2 correction of the ground state (with the prefactor $\lambda_1/2$), even without precise knowledge of the CF and HF parameters. We provide a detailed derivation thereof in the Appendix B2. Namely, we neglect the quadrupolar interaction B and restrict the sum over the CF states in Eqs. (2) and (3) to the three lowest CF states,

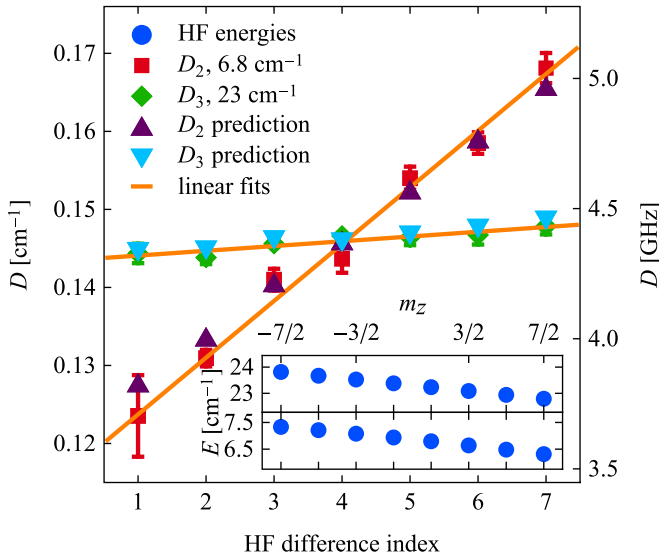


FIG. 5. Energy differences D_2 (red) and D_3 (green) between neighboring HF transitions as a function of the HF index. Linear fits to the experimental data are shown in orange. The respective slopes $s_{2,3}$ are a measure of the HF corrections $\propto m_z^2$. The numerical prediction based on our fitted CF parameters is depicted in violet and cyan. The HF transition energies are shown in the inset for the $8.1 \rightarrow 8.2$ and $8.1 \rightarrow 8.3$ transitions in the upper and lower panel, respectively.

which contribute the most to the correction. We then exploit the antisymmetry of the second-order corrections between the 8.1, 8.2, and 8.3 states to extract $\lambda_1 = (s_1 + s_2)/4 = (2.0 \pm 0.2) \times 10^{-3} \text{ cm}^{-1}$ ($60 \pm 6 \text{ MHz}$) from our data [cf. Eq. (B5)]. This is close to the numerical calculation, yielding $\lambda_1 = 0.0024 \text{ cm}^{-1}$ (72 MHz). Based on the errors found for the 8.2 and 8.3 energy-level predictions, we expect a similar error of $\lesssim 16\%$ for λ_1 . Akin to λ_1 , we estimate $\lambda_2 = (-2.5 \pm 0.1) \times 10^{-3} \text{ cm}^{-1}$ ($-75 \pm 3 \text{ MHz}$) and $\lambda_3 = (1.9 \pm 0.3) \times 10^{-3} \text{ cm}^{-1}$ ($57 \pm 9 \text{ MHz}$) by including the $8.2 \rightarrow 8.3$ transition. Both values are also in agreement with the numerical results $\lambda_2 = -0.0040 \text{ cm}^{-1}$ (-120 MHz) and $\lambda_3 = 0.0017 \text{ cm}^{-1}$ (51 MHz).

V. DISCUSSION

We compare our CF parameter values, given in Table II, with previous results [17,19,26,35–39] which we show in Fig. 7 of Appendix C. First, we consider the magnitude of our CF parameters with respect to literature values. While our values lie centered on the spread of previous predictions for B_4^4 and B_6^4 , we obtain significantly smaller or larger values for the rest. We attribute these corrections to the inclusion of the HF interaction term (to first order in A_J) in the Hamiltonian. In particular, fitting the HF structure allows us to use the magnetic moment of the 8.1 and 8.6 doublets (measured in Ref. [20]) as an additional constraint of the CF parameters, which determines the first-order HF splitting. Second, we compare predictions of key parameters such as CF energies and magnetic moments of doublet states. While we have shown in Sec. IV that our CF parameters predict the measured hyperfine-split CF energies with an accuracy limited by the

TABLE III. Calculated energy levels of Ho^{3+} in $\text{LiY}_{1-x}\text{Ho}_x\text{F}_4$ based on the CF parameters in Table II. The last column shows the expectation value J_z of the magnetic Γ_4 states, which is proportional to their longitudinal magnetic moment μ divided by the Landé g factor $g_J = \frac{5}{4}$.

CF state	Energy		Symmetry	$\langle J_z \rangle = \mu/(g_J \mu_B)$
	(cm^{-1})	(THz)		
8.1	0.00	0.000	$\Gamma_{3,4}$	5.40
8.2	6.84	0.205	Γ_2	
8.3	23.31	0.699	Γ_2	
8.4	47.60	1.427	Γ_1	
8.5	56.92	1.706	Γ_1	
8.6	72.10	2.162	$\Gamma_{3,4}$	-3.60
8.7	190.88	5.722	Γ_1	
8.8	257.47	7.719	$\Gamma_{3,4}$	-2.30
8.9	275.31	8.254	Γ_2	
8.10	275.38	8.256	Γ_1	
8.11	288.66	8.654	Γ_1	
8.12	294.65	8.833	$\Gamma_{3,4}$	4.51
8.13	303.37	9.095	Γ_2	

measurement resolution, we test the prediction of the centroid CF energy for previous sets of CF parameters. We consider the average deviation of the prediction for the 8.2 to 8.6 CF energies (given in Table IV in Appendix C) to the measurements. For any previous set of CF parameters the deviations are at least 60 times larger than ours. In addition, our predictions deviate by 2%–10% from previously predicted energies for the CF levels 8.7 to 8.13, which are not directly measurable due to phonon absorption bands [42], emphasizing the need for a precise prediction. We also find a considerably ($\sim 10\%$) smaller magnetic moment $\mu/\mu_B = \pm 4.49$ of the 8.6 states than of previous CF parameters. We show our predicted CF energies of the 5I_8 manifold and their magnetic moments in Table III. These results reveal that including HF interactions to first order in A_J leads to a significant modification of the extracted CF parameters. While alteration alone is no guarantee for correctness, we show the latter by the more precise

TABLE IV. Standard deviation $\sigma(E_{\text{CF}})$ of calculated CF energies of the 8.2 to 8.6 states and the experimental results, as well as the magnetic moments $\langle J_z \rangle$. Input are CF parameters from literature and this work. We fix $E_{\text{CF},8.1} = 0$ (cf. Table III). The expectation value $\langle J_z \rangle$ refers to the Γ_4 state of the 8.1 and 8.6 doublets.

CF parameters	$\sigma(E_{\text{CF}})$		$\langle J_z \rangle$	
	(cm^{-1})	(GHz)	8.1	8.6
Hansen 1975 [37]	6.90	206.8	5.38	-3.99
Gifeisman 1978 [35]	2.97	89.0	5.53	-3.83
Christensen 1979 [26]	2.97	89.0	5.52	-3.96
Beauvillain 1980 [38]	7.75	232.3	5.46	-4.09
Görrler-Walrand 1996 [36]	4.87	146.0	5.42	-3.97
Shakurov 2005 [17]	2.13	63.9	5.49	-3.93
Rønnow 2007 [39]	2.15	64.5	5.51	-4.02
Babkevich 2015 [19]	0.393	11.8	5.51	-3.92
This work	0.006	0.2	5.40	-3.60

reproduction of measured CF energies than any previous sets of CF parameters allow. Further studies could address the CF parameters' potentially nontrivial dependence on the doping concentration x , requiring caution when comparing CF parameters across the series $\text{LiY}_{1-x}\text{Ho}_x\text{F}_4$.

In addition to predicting CF energies, CF parameters are also required for understanding more complex properties of $\text{LiY}_{1-x}\text{Ho}_x\text{F}_4$. The energy splitting of the ground state in a transverse field is determined by admixture of low-lying CF states in the ground-state manifold. Therefore, the magnetic phase diagram (e.g., Ref. [16]) and hysteresis loops of magnetization [1] are especially sensitive to changes in CF parameters. While the prediction of the magnetic phase diagram involves additional parameters such as the exchange interaction J_{ex} , the B_z -dependent HF energies and the relaxation of magnetization via Landau-Zener tunneling depends on the quadrupole HF interaction B derived here. We exemplify this in Appendix C3 for our and previous sets of CF parameters, revealing that our predictions are consistent with existing measurements in Ref. [27]. Given that our set of CF parameters predicts the CF energies best, also our predictions of HF energy splittings (which crucially depend on B as shown in Table VI in Appendix C3) will be more precise. Finally, we expect our improved CF parameters to support further progress in understanding the equilibrium quantum statistical mechanics of $\text{LiY}_{1-x}\text{Ho}_x\text{F}_4$ as well as driven off-equilibrium protocols [1,10–12] via a more precise modeling of the low-energy Hamiltonian.

VI. CONCLUSIONS

In summary, we have precisely determined the low-energy electronuclear Hamiltonian of $\text{LiY}_{1-x}\text{Ho}_x\text{F}_4$, thus providing a starting point to further deepen the understanding of the system, most notably the mapping to the simple transverse field Ising model, across a large range of dilution series. We have extended the characterization of the ground CF state manifold of $\text{LiY}_{1-x}\text{Ho}_x\text{F}_4$ ($x = 1\%$, 0.1% , and 0.01%) by optical measurements of transitions within the lowest three CF states. From the data we have calculated the CF parameters, which differ from previous estimates because our refinement also considers the magnetic moments of the CF states as an additional fit constraint via the first-order HF shift in A_J . This enabled us to deduce the dipolar HF constant $A_J = 0.02703 \pm 0.00003 \text{ cm}^{-1}$ ($810.3 \pm 0.9 \text{ MHz}$) by optical means. From the CF parameters we derive the energies for the CF states of the 5J_8 ground-state manifold. We benchmark the precision of our calculated CF energies which yields a 60 times more accurate result than using previous CF parameter sets. Our high-measurement resolution also allowed us to determine the quadrupolar HF constant $B = 0.04 \pm 0.01 \text{ cm}^{-1}$ ($1.2 \pm 0.3 \text{ GHz}$) and subsequently to calculate the HF corrections of the three lowest CF states. We corroborate these calculations via estimating the same corrections directly from our data. Further, we report in Appendix A the far-infrared refractive index of $\text{LiY}_{1-x}\text{Ho}_x\text{F}_4$.

ACKNOWLEDGMENTS

FTIR spectroscopy data were taken at the X01DC beamline of the Swiss Light Source, Paul Scherrer Institut, Villigen,

Switzerland. We thank H. M. Rønnow, P. Babkevich, and J. Bailey for helpful discussions and experimental support. We thank S. Stutz for technical support at the X01DC beamline. We acknowledge financial support by the Swiss National Science Foundation, Grant No. 200021_166271, the European Research Council under the European Union's Horizon 2020 research and innovation programme HERO (Grant Agreement No. 810451), and the Engineering and Physical Sciences Research Council, U.K. ("HyperTerahertz" Grant No. EP/P021859/1 and "COTS" Grant No. EP/J017671/1).

APPENDIX A: REFRACTIVE INDEX IN THE FAR INFRARED

We report the frequency-dependent ordinary refractive index n_o of $\text{LiY}_{1-x}\text{Ho}_x\text{F}_4$ in the FIR regime $10 \lesssim \tilde{\nu} \lesssim 70 \text{ cm}^{-1}$ ($0.3 \lesssim \nu \lesssim 2.1 \text{ THz}$). Figure 6 shows $n_o(\nu)$ of a 2.07-mm-thick $x = 1\%$ crystal for $T = 100$ and 6 K, as measured with TDS, where the THz electric field is polarized perpendicular to the crystallographic c axis (the optic axis lies along crystallographic c axis). The results have been obtained from the complex transmission of the sample, calculated from the Fourier transforms of the measured time-domain signals with and without the crystal in the cryostat. The index is then given by $n = c \times \delta\phi / (\omega L) + n_{\text{air}}$, where c is the speed of light, ω the angular frequency, L is the thickness of the sample, $n_{\text{air}} = 1$ is the refractive index of air, and $\delta\phi$ is the phase difference, obtained from the complex transmission. We fit a phenomenological model $n_o(\tilde{\nu}) = a / (\tilde{\nu} - \tilde{\nu}_0) + c$ to the data, motivated by the divergence of the refractive index near zone-center phonons around $\tilde{\nu}_0 = 150 \text{ cm}^{-1}$ [42]. From a least-squares fit we find $c = 2.62 \pm 0.01$ for both temperatures, $a_{6\text{K}} = -11.1 \pm 0.9 \text{ cm}^{-1}$, $a_{100\text{K}} = -13.5 \pm 0.5 \text{ cm}^{-1}$, $\tilde{\nu}_{0,6\text{K}} = 110 \pm 2 \text{ cm}^{-1}$, and $\tilde{\nu}_{0,100\text{K}} = 115 \pm 1 \text{ cm}^{-1}$.

APPENDIX B: HYPERFINE ENERGIES

1. Perturbation theory

The dipolar and quadrupolar HF interaction Hamiltonian is given in Eq. (1). Rewriting this Hamiltonian in terms of

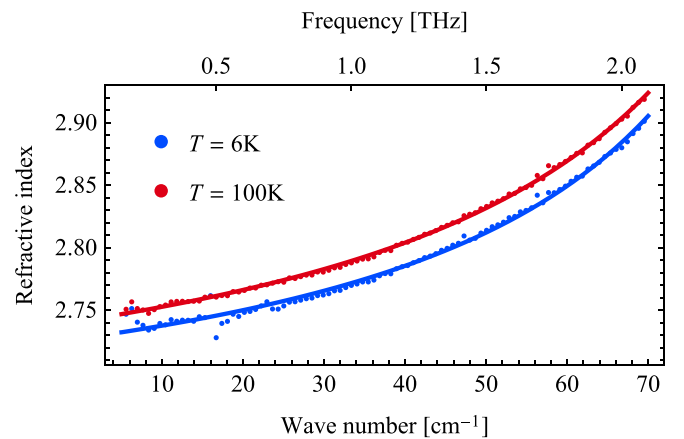


FIG. 6. The ordinary refractive index of $\text{LiY}_{1-x}\text{Ho}_x\text{F}_4$ ($x = 1\%$) measured at temperatures of $T = 100$ and 6 K is shown in red and blue, respectively. Solid lines denote fits to the phenomenological model.

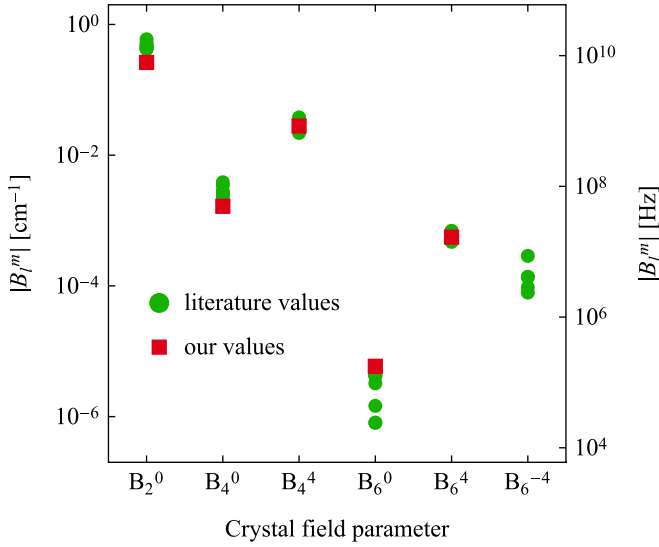


FIG. 7. Absolute value of CF parameters in literature (green, Refs. [17,19,26,35–39]) compared to this work (red) on logarithmic scale. We find $B_6^0 \approx 0$ (cf. Table II in the main text).

the operators J_z, J_+, J_- and I_z, I_+, I_- allows us to derive the perturbative second-order energy corrections in A_J and first-order ones in B as

$$\begin{aligned} \delta_{8.n^\sigma, m_z} = & A_J \langle 8.n^\sigma | J_z | 8.n^\sigma \rangle m_z \\ & + \sum_{j \neq n} \sum_{\sigma' = \pm} \frac{A_J^2}{\Delta E_{ij}} \left[|\langle 8.j^\sigma | J_z | 8.n^\sigma \rangle|^2 m_z^2 \right. \\ & + \frac{1}{4} |\langle 8.j^{\sigma'} | J_- | 8.n^\sigma \rangle|^2 [I(I+1) - m_z(m_z+1)] \\ & + \frac{1}{4} |\langle 8.j^{\sigma'} | J_+ | 8.n^\sigma \rangle|^2 [I(I+1) - m_z(m_z-1)] \left. \right] \\ & + \frac{B \langle 8.n^\sigma | 3J_z^2 - J(J+1) | 8.n^\sigma \rangle}{4I(2I-1)J(2J-1)} [3m_z^2 - I(I+1)]. \end{aligned} \quad (\text{B1})$$

We have already used the fact here that, owing to the S_4 crystal symmetry of LiYF_4 , the expectation value of the angular momentum operators with the CF states can only be nonzero for the J_z component, and similarly only the J_z^2 component of the quadrupole operators.

The S_4 and time-reversal symmetries simplify the expression (B1) even further since most of the matrix elements vanish. Due to time-reversal symmetry, the first-order correction in A_J is only nonzero for CF doublets, e.g., levels 8.1 and 8.6. Owing to the S_4 crystal symmetry [with the symmetry operator being $U = \exp(i\frac{\pi}{4}J_z)$], the matrix elements $\langle 8.j^\sigma | J_z | 8.i^\sigma \rangle$ of the second-order corrections in A_J are finite only if the states $|8.i\rangle$ and $|8.j\rangle$ carry the same irreducible representation. Furthermore, $\langle 8.i^\sigma | J_+ | 8.j^{\sigma'} \rangle$ is nonzero only for matrix elements between pairs of states $\langle \Gamma_1 | J_+ | \Gamma_3 \rangle$, $\langle \Gamma_3 | J_+ | \Gamma_2 \rangle$, $\langle \Gamma_2 | J_+ | \Gamma_4 \rangle$, $\langle \Gamma_4 | J_+ | \Gamma_1 \rangle$, and, with i and j exchanged, for the Hermitian conjugate matrix elements $\langle 8.i^\sigma | J_+ | 8.j^{\sigma'} \rangle^\dagger = \langle 8.j^{\sigma'} | J_- | 8.i^\sigma \rangle$ as $J_- = J_+^\dagger$. Here, $|\Gamma_i\rangle$ stands for any CF state that transforms as Γ_i . Using these

symmetry constraints in Eq. (B1), we arrive at Eqs. (2) and (3).

2. Extraction of the ground-state HF corrections

In the following we restrict the sum over CF states in Eq. (B1) to the lowest three CF states 8.1, 8.2, and 8.3. This is motivated by the fact that these states give the dominant contributions in the second-order corrections of A_J due to the small energy denominators. Further, here we neglect the quadrupolar coupling B , which enables us to estimate the ground-state HF energies from our data without prior knowledge of the CF parameters or the constant A_J .

Taking into account this reduced Hilbert space of only the three lowest CF states, the energy corrections $\delta_{8.i^\sigma, m_z}$ up to second order in A_J can be written as

$$\begin{aligned} \delta_{8.1^+, m_z} = & \delta_{8.1^-, -m_z} \\ = & K_{1,1}(m_z) + K_{1,2}(m_z) + K_{1,3}(m_z), \end{aligned} \quad (\text{B2})$$

$$\delta_{8.2, \pm m_z} = K_{2,3}(m_z) + 2K_{2,1}(m_z),$$

$$\delta_{8.3, \pm m_z} = K_{3,2}(m_z) + 2K_{3,1}(m_z),$$

where $K_{i,j}$ defines the perturbative energy correction of level i due to the level j :

$$\begin{aligned} K_{1,1}(m_z) = & A_J \langle 8.1^+ | J_z | 8.1^+ \rangle m_z, \\ K_{1,i=2,3}(m_z) = & \frac{A_J^2}{4} \frac{|\langle 8.i | J_- | 8.1^+ \rangle|^2}{\Delta E_{1i}} \\ & \times [I(I+1) - m_z(m_z+1)], \quad (\text{B3}) \\ K_{2,3}(m_z) = & \frac{A_J^2}{\Delta E_{23}} |\langle 8.3 | J_z | 8.2 \rangle|^2 m_z^2, \\ K_{i,j \neq i}(m_z) = & -K_{j,i}(m_z). \end{aligned}$$

Measured transitions between the 8.1, 8.2, and 8.3 states (with m_z conserved) then allow us to extract the second-order ground state HF corrections in A_J , i.e., $K_{1,2}(m_z) + K_{1,3}(m_z)$. We use the antisymmetry of $K_{i,j \neq i}(m_z)$ in Eq. (B3) to cancel out the contributions $K_{2,3}(m_z)$ in the transition frequencies. We do this by using the differences $D_i(m_z)$ ($i = 2, 3$) of transition frequencies $8.1 \rightarrow 8.i$ between neighboring m_z :

$$\begin{aligned} D_i(m_z) = & (\delta_{8.i, m_z+1} - \delta_{8.1^+, m_z+1}) \\ & - (\delta_{8.i, m_z} - \delta_{8.1^+, m_z}). \end{aligned} \quad (\text{B4})$$

The purely electronic CF transition energies cancel out in $D_i(m_z)$ when we take the difference of two transitions. We add $D_2(m_z)$ and $D_3(m_z)$ to eliminate the contributions $K_{2,3}(m_z)$ and $K_{3,2}(m_z)$ (due to the antisymmetry of K). Taking the difference between neighboring m_z , we recover the coefficient of the $\propto m_z^2$ correction in Eqs. (B2) and (B3). We introduce λ_1 which is twice this coefficient:

$$\begin{aligned} \lambda_1 = & \frac{d\delta_{8.1^+, m_z}}{dm_z} = \frac{d}{dm_z} [K_{1,2}(m_z) + K_{1,3}(m_z)] \\ = & -\frac{1}{4} [D_2(m_z+1) + D_3(m_z+1)] \\ & - [D_2(m_z) + D_3(m_z)]. \end{aligned} \quad (\text{B5})$$

The energy difference between neighboring $m_z \rightarrow m_z + 1$ transitions within the ground-state doublet is given by λ_1 . Its

TABLE V. Calculated HF energies $E_{8.1^+, m_z} - E_{8.1^+, -7/2}$ of the $|8.1^+, I_z\rangle$ states with with $A = 0.0270 \text{ cm}^{-1}$ and with $B = 0.0374 \text{ cm}^{-1}$.

Ref.	$m_z = -5/2$		$m_z = -3/2$		$m_z = -1/2$		$m_z = +1/2$		$m_z = +3/2$		$m_z = +5/2$		$m_z = +7/2$	
	(cm^{-1})	(GHz)	(cm^{-1})	(GHz)	(cm^{-1})	(GHz)	(cm^{-1})	[GHz]	(cm^{-1})	(GHz)	(cm^{-1})	(GHz)	(cm^{-1})	(GHz)
[37]	0.139	4.16	0.28	8.38	0.424	12.7	0.569	17.1	0.717	21.5	0.868	26.0	1.02	30.6
[35]	0.144	4.32	0.29	8.69	0.438	13.1	0.588	17.6	0.739	22.2	0.893	26.8	1.05	31.5
[26]	0.143	4.29	0.288	8.64	0.436	13.1	0.585	17.5	0.736	22.1	0.890	26.7	1.05	31.4
[38]	0.141	4.24	0.285	8.54	0.431	12.9	0.579	17.3	0.729	21.8	0.881	26.4	1.04	31.1
[36]	0.141	4.21	0.283	8.48	0.428	12.8	0.575	17.2	0.724	21.7	0.875	26.2	1.03	30.9
[17]	0.142	4.25	0.286	8.57	0.433	13.0	0.581	17.4	0.732	22.0	0.886	26.6	1.04	31.2
[39]	0.143	4.28	0.288	8.62	0.435	13.0	0.584	17.5	0.736	22.1	0.890	26.7	1.05	31.4
[19]	0.142	4.27	0.287	8.60	0.434	13.0	0.583	17.5	0.735	22.0	0.889	26.6	1.05	31.4
This work	0.140	4.18	0.281	8.42	0.425	12.8	0.571	17.1	0.720	21.6	0.871	26.1	1.02	30.7

value is estimated in the main text by fitting linear functions to $D_i(m_z)$.

Similarly, we determine the coefficients of the m_z^2 - HF correction in the 8.2 and 8.3 states, λ_2 and λ_3 , respectively, as

$$\lambda_2 = \frac{1}{4}[D_2(m_z + 1) + D_3(m_z + 1) - 2D_1(m_z + 1) - [D_2(m_z) + D_3(m_z) - 2D_2(m_z + 1)]] \quad (\text{B6})$$

and

$$\lambda_3 = \frac{1}{4}[D_2(m_z + 1) + D_3(m_z + 1) + 2D_1(m_z + 1) - [D_2(m_z) + D_3(m_z) + 2D_2(m_z + 1)]], \quad (\text{B7})$$

where we defined the difference $D_1(m_z)$ of transition frequencies 8.2 \rightarrow 8.3 between neighboring m_z as

$$D_1(m_z) = (\delta_{8.3, m_z+1} - \delta_{8.2, m_z+1}) - (\delta_{8.3, m_z} - \delta_{8.2, m_z}). \quad (\text{B8})$$

APPENDIX C: COMPARISON OF CRYSTAL-FIELD PARAMETERS TO LITERATURE

We illustrate the comparison of our CF parameters to literature values in Fig. 7. While some properties of the CF states are rather insensitive to changes of the CF parameters, others can change drastically, requiring a more refined set of CF parameters and more detailed description of the dipolar and quadrupolar hyperfine interaction. Here we compare some

properties of the CF states in the 5I_8 manifold as calculated with various CF parameters. Some of these properties have not been measured directly and, thus, serve as predictions for future experiments, which in turn could again further refine the parameters.

1. CF energies and magnetic moments

We compare the magnetic moments and the deviation of the (mean) CF energies 8.2 \rightarrow 8.6 for various CF parameters in Table IV. The experimental values of the energies for the states 8.2 and 8.3 were extracted from the data in the main text. The 8.4 \rightarrow 8.6 energies were deduced from Ref. [20] (using the mean energy wherever several transition frequencies are tabulated).

2. Ground-state HF energies

In Table V we summarize the ground-state (8.1) HF energies for literature values of CF parameters in the absence of an external field.

3. Landau-Zener tunneling

Giraud *et al.* [1] measured staircaselike hysteresis loops of the Ho magnetization in $\text{LiY}_{1-x}\text{Ho}_x\text{F}_4$ ($x = 0.2\%$). These are caused by thermally activated quantum tunneling at avoided crossings of the Ho hyperfine states. At very low temperatures

TABLE VI. Gap ΔE of the avoided $|8.1^+, -\frac{7}{2}\rangle$ and $|8.1^-, \frac{5}{2}\rangle$ crossing (columns 2 to 5) and gap of the avoided $|8.1^+, -\frac{1}{2}\rangle$ and $|8.1^-, \frac{3}{2}\rangle$ (columns 6 to 9) at $B_z \approx 230 \text{ G}$ calculated for various CF parameters. We use the quadrupolar HF interaction B as extracted in the main text.

CF parameters	ΔE of $ 8.1^+, -\frac{7}{2}\rangle$ and $ 8.1^-, \frac{5}{2}\rangle$				ΔE of $ 8.1^+, -\frac{1}{2}\rangle$ and $ 8.1^-, \frac{3}{2}\rangle$			
	$B = 0 \text{ cm}^{-1}$		$B = 0.04 \text{ cm}^{-1}$		$B = 0 \text{ cm}^{-1}$		$B = 0.04 \text{ cm}^{-1}$	
	(10^{-8} cm^{-1})	(kHz)	(10^{-8} cm^{-1})	(kHz)	(10^{-8} cm^{-1})	(Hz)	(10^{-8} cm^{-1})	(Hz)
Hansen 1975 [37]	5.06	1.52	4.39	1.32	1.77	532	1.65	495
Gifeisman 1978 [35]	0.0324	0.00972	0.802	0.240	0.698	209	0.666	200
Christensen 1979 [26]	0.0467	0.0140	1.50	0.451	0.952	285	0.916	275
Beauvillain 1980 [38]	1.87	0.561	2.25	0.673	1.26	377	1.19	355
Görrler-Walrand 1996 [36]	0.685	0.205	2.56	0.769	1.32	395	1.22	367
Shakurov 2005 [17]	2.50	0.749	2.52	0.755	1.37	411	1.28	383
Rønnow 2007 [39]	1.50	0.449	1.96	0.588	1.20	361	1.12	336
Babkevich 2015 [19]	4.14	1.24	2.35	0.703	1.44	432	1.30	390
This work	0.159	0.0477	3.13	0.938	1.41	422	1.33	400

(below those in Ref. [1]), it is expected that the relaxation of the magnetization (after crossing the zero field) is dominated by direct Landau-Zener tunneling at $B_z \approx 230$ G, where the states $|8.1^+, -\frac{7}{2}\rangle$ and $|8.1^-, \frac{5}{2}\rangle$ have an avoided crossing. This gap appears only in sixth-order perturbation theory (of the transverse hyperfine interaction) and is thus quite small. Furthermore, the gap-opening term contains matrix elements with possible pathways via the two Γ_1 states 8.4 and 8.5. It turns out that these two matrix elements interfere nearly destructively such that a change in these matrix elements has a huge effect on the size of the gap (several orders of magnitude) and thus the relaxation timescale. In Table VI, we compare

the size of this gap for literature values of CF parameters both with and without quadrupolar hyperfine interactions.

At higher temperatures, it is expected that the relaxation of the magnetization (after crossing the zero field) is dominated at multiples of $B_z \approx n \times 230$ G ($n \in [\pm 1, \pm 2, \pm 3]$), where hyperfine states with Δm_z have avoided crossings. Therefore, we also compare the size of the gap between the states $|8.1^+, -\frac{1}{2}\rangle$ and $|8.1^-, \frac{3}{2}\rangle$ (at $B_z = 230$ G) for various CF parameters both with and without quadrupolar hyperfine interactions in Table VI, columns 6–9. The experimental value of $\Delta E = 0.015$ cm⁻¹ (with a resolution of 0.002 cm⁻¹) was measured in Ref. [27] and is consistent with our CF parameters.

-
- [1] R. Giraud, W. Wernsdorfer, A. M. Tkachuk, D. Maily, and B. Barbara, Nuclear Spin Driven Quantum Relaxation in LiY_{0.998}Ho_{0.002}F₄, *Phys. Rev. Lett.* **87**, 057203 (2001).
- [2] H. M. Rønnow, R. Parthasarathy, J. Jensen, G. Aeppli, T. F. Rosenbaum, and D. F. McMorrow, Quantum phase transition of a magnet in a spin bath, *Science* **308**, 389 (2005).
- [3] D. Bitko, T. F. Rosenbaum, and G. Aeppli, Quantum Critical Behavior for a Model Magnet, *Phys. Rev. Lett.* **77**, 940 (1996).
- [4] W. Wu, B. Ellman, T. F. Rosenbaum, G. Aeppli, and D. H. Reich, From Classical to Quantum Glass, *Phys. Rev. Lett.* **67**, 2076 (1991).
- [5] C. Ancona-Torres, D. M. Silevitch, G. Aeppli, and T. F. Rosenbaum, Quantum and Classical Glass Transitions in LiHo_xY_{1-x}F₄, *Phys. Rev. Lett.* **101**, 057201 (2008).
- [6] W. Wu, D. Bitko, T. F. Rosenbaum, and G. Aeppli, Quenching of the Nonlinear Susceptibility at a $T = 0$ Spin Glass Transition, *Phys. Rev. Lett.* **71**, 1919 (1993).
- [7] J. Brooke, T. F. Rosenbaum, and G. Aeppli, Tunable quantum tunnelling of magnetic domain walls, *Nature (London)* **413**, 610 (2001).
- [8] D. M. Silevitch, D. Bitko, J. Brooke, S. Ghosh, G. Aeppli, and T. F. Rosenbaum, A ferromagnet in a continuously tunable random field, *Nature (London)* **448**, 567 (2007).
- [9] S. Ghosh, T. F. Rosenbaum, G. Aeppli, and S. N. Coppersmith, Entangled quantum state of magnetic dipoles, *Nature (London)* **425**, 48 (2003).
- [10] S. Ghosh, R. Parthasarathy, T. F. Rosenbaum, and G. Aeppli, Coherent spin oscillations in a disordered magnet, *Science* **296**, 2195 (2002).
- [11] M. A. Schmidt, D. M. Silevitch, G. Aeppli, and T. F. Rosenbaum, Using thermal boundary conditions to engineer the quantum state of a bulk magnet, *Proc. Natl. Acad. Sci. USA* **111**, 3689 (2014).
- [12] D. M. Silevitch, C. Tang, G. Aeppli, and T. F. Rosenbaum, Tuning high- Q nonlinear dynamics in a disordered quantum magnet, *Nat. Commun.* **10**, 4001 (2019).
- [13] J. Brooke, D. Bitko, T. F. Rosenbaum, and G. Aeppli, Quantum annealing of a disordered magnet, *Science* **284**, 779 (1999).
- [14] A. Dutta, G. Aeppli, B. Chakrabarti, U. Divakaran, T. Rosenbaum, and D. Sen, *Quantum Phase Transitions in Transverse Field Models* (Cambridge University Press, Cambridge, 2015).
- [15] H. Kjønsgberg and S. M. Girvin, The classical phase transition in LiHoF₄: Results from mean field theory and monte carlo simulations, in *Fundamental Physics Of Ferroelectrics 2000, AIP Conference Proceedings Volume 535*, edited by R. E. Cohen and R. A. Mewaldt (AIP, Melville, NY, 2000), p. 323.
- [16] P. B. Chakraborty, P. Henelius, H. Kjønsgberg, A. W. Sandvik, and S. M. Girvin, Theory of the magnetic phase diagram of LiHoF₄, *Phys. Rev. B* **70**, 144411 (2004).
- [17] G. S. Shakhurov, M. V. Vanyunin, B. Z. Malkin, B. Barbara, R. Y. Abdulsabirov, and S. L. Korableva, Direct measurements of anticrossings of the electron-nuclear energy levels in LiYF₄ : Ho³⁺ with submillimeter EPR spectroscopy, *Appl. Magn. Reson.* **28**, 251 (2005).
- [18] G. S. Shakhurov, B. Z. Malkin, M. V. Vanyunin, and S. L. Korableva, Multi-range high-frequency EPR spectroscopy of LiYF₄ and LiLuF₄ crystals doped by rare-earth ions, *Phys. Solid State* **50**, 1619 (2008).
- [19] P. Babkevich, A. Finco, M. Jeong, B. Dalla Piazza, I. Kovacevic, G. Klughertz, K. W. Krämer, C. Kraemer, D. T. Adroja, E. Goremychkin, T. Unruh, T. Strässle, A. Di Lieto, J. Jensen, and H. M. Rønnow, Neutron spectroscopic study of crystal-field excitations and the effect of the crystal field on dipolar magnetism in LiRF₄ ($R = \text{Gd, Ho, Er, Tm, and Yb}$), *Phys. Rev. B* **92**, 144422 (2015).
- [20] G. Matmon, S. A. Lynch, T. F. Rosenbaum, A. J. Fisher, and G. Aeppli, Optical response from terahertz to visible light of electronuclear transitions in LiYF₄ : Ho³⁺, *Phys. Rev. B* **94**, 205132 (2016).
- [21] B. Bleaney, in *Magnetic Properties of Rare Earth Metals*, edited by R. J. Elliott (Springer, Boston, MA, 1972).
- [22] N. Agladze and M. Popova, Hyperfine structure in optical spectra of LiYF₄-Ho, *Solid State Commun.* **55**, 1097 (1985).
- [23] M. J. P. Gingras and P. Henelius, Collective phenomena in the LiY_{1-x}Ho_xF₄ quantum ising magnet: Recent progress and open questions, *J. Phys.: Conf. Ser.* **320**, 012001 (2011).
- [24] S. Albert, K. K. Albert, P. Lerch, and M. Quack, Synchrotron-based highest resolution Fourier transform infrared spectroscopy of naphthalene (C₁₀H₈) and indole (C₈H₇N) and its application to astrophysical problems, *Faraday Discuss.* **150**, 71 (2011).
- [25] N. Karayianis, D. Wortman, and H. Jenssen, Analysis of the optical spectrum of Ho³⁺ in LiYF₄, *J. Phys. Chem. Solids* **37**, 675 (1976).
- [26] H. P. Christensen, Spectroscopic analysis of LiHoF₄ and LiErF₄, *Phys. Rev. B* **19**, 6564 (1979).

- [27] K. N. Boldyrev, M. N. Popova, B. Z. Malkin, and N. M. Abishev, Direct observation of hyperfine level anticrossings in the optical spectra of a ${}^7\text{LiYF}_4 : \text{Ho}^{3+}$ single crystal, *Phys. Rev. B* **99**, 041105(R) (2019).
- [28] A. Beckert, H. Sigg, and G. Aeppli, Taking advantage of multiplet structure for lineshape analysis in fourier space, *Opt. Express* **28**, 24937 (2020).
- [29] A. Abragam and B. Bleaney, *Electron Paramagnetic Resonance of Transition Ions*, International Series of Monographs on Physics (Clarendon, Oxford, 1970).
- [30] N. I. Agladze, E. A. Vinogradov, and M. N. Popova, Manifestation of quadrupole hyperfine interaction and of interlevel interaction in the optical spectrum of the $\text{LiYF}_4 : \text{Ho}$ crystal, *Zh. Eksp. Teor. Fiz.* **91**, 1210 (1986) [*JETP* **64**, 716 (1986)].
- [31] M. N. Popova, E. P. Chukalina, B. Z. Malkin, and S. K. Saikin, Experimental and theoretical study of the crystal-field levels and hyperfine and electron-phonon interactions in $\text{LiYF}_4 : \text{Er}^{3+}$, *Phys. Rev. B* **61**, 7421 (2000).
- [32] N. I. Agladze, M. N. Popova, G. N. Zhizhin, V. J. Egorov, and M. A. Petrova, Isotope Structure In Optical Spectra of $\text{LiYF}_4 : \text{Ho}^{3+}$ *Phys. Rev. Lett.* **66**, 477 (1991).
- [33] N. I. Agladze, M. N. Popova, M. A. Koreiba, B. Z. Malkin, and V. R. Pekurovskii, Isotope effects in the lattice structure and vibrational and optical spectra of ${}^6\text{Li}_x{}^7\text{Li}_{1-x}\text{YF}_4 : \text{Ho}$ crystals, *Zh. Eksp. Teor. Fiz.* **104**, 4171 (1993) [*JETP* **77**, 1021 (1993)].
- [34] F. Könz, Y. Sun, C. W. Thiel, R. L. Cone, R. W. Equall, R. L. Hutchison, and R. M. Macfarlane, Temperature and concentration dependence of optical dephasing, spectral-hole lifetime, and anisotropic absorption in $\text{Eu}^{3+} : \text{Y}_2\text{SiO}_5$, *Phys. Rev. B* **68**, 085109 (2003).
- [35] S. N. Gifeisman, A. M. Tkachuk, and V. V. Prizmak, Optical spectra of Ho^{3+} ion in LiYF_4 crystals, *Opt. Spectrosc.* **44**, 120 (1978).
- [36] C. Görrler-Walrand and K. Binnemans, Rationalization of crystal-field parametrization, in *Handbook on the Physics and Chemistry of Rare Earths*, Vol. 23 (Elsevier, Amsterdam, 1996), Chap. 155 pp. 121–283.
- [37] P. E. Hansen, T. Johansson, and R. Nevald, Magnetic properties of lithium rare-earth fluorides: Ferromagnetism in LiErF_4 and LiHoF_4 and crystal-field parameters at the rare-earth and li sites, *Phys. Rev. B* **12**, 5315 (1975).
- [38] P. Beauvillain, C. Chappert, and I. Laursen, Critical behaviour of the magnetic susceptibility at marginal dimensionality in LiTbF_4 , *J. Phys. C: Solid State Phys.* **13**, 1481 (1980).
- [39] H. M. Rønnow, J. Jensen, R. Parthasarathy, G. Aeppli, T. F. Rosenbaum, D. F. McMorrow, and C. Kraemer, Magnetic excitations near the quantum phase transition in the ising ferromagnet LiHoF_4 , *Phys. Rev. B* **75**, 054426 (2007).
- [40] J. Magariño, J. Tuchendler, P. Beauvillain, and I. Laursen, EPR experiments in LiTbF_4 , LiHoF_4 , and LiErF_4 at submillimeter frequencies, *Phys. Rev. B* **21**, 18 (1980).
- [41] G. Mennenga, L. de Jongh, and W. Huiskamp, Field dependent specific heat study of the dipolar ising ferromagnet LiHoF_4 , *J. Magn. Magn. Mater.* **44**, 59 (1984).
- [42] S. Salaün, M. T. Fornoni, A. Bulou, M. Rousseau, P. Simon, and J. Y. Gesland, Lattice dynamics of fluoride scheelites: I. Raman and infrared study of LiYF_4 and LiLnF_4 ($\text{Ln} = \text{Ho}, \text{Er}, \text{Tm}$ and Yb), *J. Phys.: Condens. Matter* **9**, 6941 (1997).